


In-Air Microfluidic Strategy for the Production of Sodium Alginate Fibers with Regular Inclusions at Very High Throughput

Francesco Marangon[✉], David Baumgartner[✉], and Carole Planchette^{✉*}

Institute of Fluid Mechanics and Heat Transfer, Graz University of Technology, Graz A-8010, Austria

 (Received 10 August 2022; revised 7 February 2023; accepted 1 March 2023; published 2 May 2023)

Scalable technologies for the production of biocompatible complex microfibers of controllable size and composition at competitively high throughput are urgently needed in order to meet the growing demand for such microstructures in pharmaceutical and biomedical applications. Here, we introduce an in-air microfluidic strategy with throughput greater than 1400 ml h^{-1} (corresponding to more than 17 000 m of fiber per hour). The microfibers of uniform diameter have regular inclusions, which can potentially be used for encapsulating cells into a protecting and nutrient environment, or for finely tuning the release of various actives at individualized doses. With the help of a recently developed prototype, we test seven different liquid combinations and obtain seven types of fibers, whose average “dry” diameter ranges between $94 \mu\text{m}$ and $170 \mu\text{m}$. The principle of our approach is to solidify the complex liquid structures generated by the controlled collisions of a drop stream with a continuous liquid jet, in air, via ionic cross-linking. After the stream of water-based droplets, which constitute the inclusions, collides in-air with the alginate-based jet (jet 1), the generated *drops-in-jet* compound is brought into contact with a second jet (jet 2) containing divalent cations (Sr^{2+} or Ca^{2+}) to initiate the solidification. Finally, the fibers are collected “on the fly” via a horizontal spinning plate, allow to dry (i.e., to fully equilibrate under controlled conditions), and characterized by their elongation at break and Young’s modulus.

DOI: [10.1103/PhysRevApplied.19.054006](https://doi.org/10.1103/PhysRevApplied.19.054006)

I. INTRODUCTION

Regenerative medicine aims to replace diseased or injured tissues, organs, or parts thereof so that almost any injury or degenerative disease can be cured [1]. Despite significant advances in recent decades, several problems must still be solved before this long-held dream approaches reality [2,3]. During this challenging journey toward the successful graft of organ substitutes, ideas have emerged, the realization of which promises groundbreaking medical and pharmaceutical progress. The development of *ex-vivo* models to mimic human organs is one of them. Beyond their use for fundamental research into therapeutic approaches, *ex-vivo* models can avoid animal testing and bridge the interspecies gap in implementation [4]. Another crucial need, which has attracted much attention, is the development of screening platforms to test drug efficacy or toxicity on cells. The motivation is obvious since achieving this would considerably accelerate drug discovery [5].

Such platforms could also be used for diagnostic purposes, for example to identify the antibiotic adapted to a given bacterial infection. It is in this context that this paper’s proposed approach for the production of hydrogel fibers finds its motivation. To better understand the unique advantages of our in-air microfluidic strategy over existing methods, it is essential to first summarize the requirements associated with the two previously mentioned applications, namely the elaboration of *ex-vivo* organ models and the development of an effective (cell) screening platform.

For both, the main challenges are of three types and concern (i) the encapsulation of cells or actives, (ii) the manipulability and traceability of the resulting inclusions, and, even if not purely scientific in nature, (iii) the associated throughput and cost [1]. Regarding (i), it is essential that the immediate environment of the cells (or actives) mimic the natural conditions to which they would be exposed *in vivo*. For actives, the difficulty lies in finding materials that are biocompatible, biodegradable and enable molecular diffusion with their surroundings. Moreover, for cells to grow and proliferate, it is necessary to support inter-cell exchanges and exchanges between the individual cells and the extracellular matrix. The former type of exchange is needed for the cells to self-organize and can only be initiated in three-dimensional cell clusters, as

*carole.planchette@tugraz.at

Published by the American Physical Society under the terms of the [Creative Commons Attribution 4.0 International](https://creativecommons.org/licenses/by/4.0/) license. Further distribution of this work must maintain attribution to the author(s) and the published article’s title, journal citation, and DOI.

opposed to two-dimensional structures [6]. Consequently, drops and beads have appeared as promising microincubators for various cell cultures [7,8]. Exchanges of the second type ensure the supply of nutrients and the elimination of waste produced by the cells. Thus, the cells must be incorporated into a porous and water-based material, whose geometry and dimensions approach those naturally encountered *in vivo*, ruling out molding approaches [9]. Alginate, a natural porous hydrogel whose gelation can be triggered via an ionic sol-gel transition, has proven its suitability [10–12] and is therefore a promising material for our applications.

At this stage, it is important to specify what is meant by the manipulability and traceability of the encapsulated cells or actives [point (ii)]. To build *ex-vivo* organ models, it is crucial to assemble various types of cells in three dimensions. While bottom-up approaches have long been proposed [13], no reliable and scalable method has been reported for microbeads [14]. In contrast, promising results have been obtained with fibers [15]. Regarding drug screening, neither beads nor standard fibers seem to have delivered satisfying results to date. More precisely, for beads to be traceable, a library must be elaborated prior to any test and then be read together with the screening results, a rather fastidious task [8]. To avoid this hurdle, it is possible simply to conserve the sequence of drops or beads via their storage in long tubing [16]. Yet, several drawbacks have limited this approach. Cross-contamination via the coalescence or fragmentation of drops and via wall wetting is a major concern [17,18]. Further, the risk of clogging [19], which increases with cells or micro-organism cultures [20] is important. Moreover, in this form, the approach is limited to short incubation periods as the exchanges between the drops (containing the cells) and the carrying immiscible phase (e.g., mineral oil) are insufficient to avoid the fatal accumulation of toxins in the cells [21]. To overcome this issue, the drops can be kept in place in the form of arrays of hanging drops [7]. Yet, such arrays require complex interfacing and are subjected to cross contamination. Finally, performing screening on fibers seems to cause more problems than it solves as the produced fiber must first be cut in elementary samples before screening can take place [22]. From this brief review, it appears that the ideal structure for drug screening should combine traceability (i.e., the possibility to identify individual samples) with their manipulability (i.e., the possibility to control their spatial arrangement to subject them to different local environments). Thus, the characteristics of the continuous fibers produced by our method, and more particularly the presence of similar but physically and regularly spaced inclusions of at least 100 μm in a mechanically robust matrix made of alginate, constitute, by design, a true solution to point (ii). We are not aware that fibers presenting these attributes have ever been produced. To obtain this unique geometry, we make use

of our knowledge of in-air microfluidics (IAMF) [23]. In brief, droplets first collide in air with a continuous liquid jet, in which they become engulfed. The resulting structure, called *drops-in-jet*, is then solidified “on the fly” via a sol-gel transition. The droplets form the regular inclusions and the jet, the hydrogel matrix in which they are embedded.

Before entering into further technical considerations (see Sec. II A), it is essential to evaluate the potential of our approach to be translated from our academic laboratory into pharmaceutical and medical progress for all. On this long and difficult journey, economically driven actors play an important role, which explains why excessively high costs and low throughput constitute the most common bottlenecks [6]. In this study, fibers can be produced with a throughput of approximately 1400 ml h^{-1} (17 000 m of fiber per hour), which is orders of magnitude greater than those achieved by classical on-chip microfluidics [typically $O(1) \mu\text{l h}^{-1}$] [24] or by microfluidics assisted approaches [up to $O(10) \text{ml h}^{-1}$] [25]. Other faster additive manufacturing methods, based on lithography or holography, have been proposed [26]. Yet, beside the toxicity of the required photoinitiators and the deleterious effects of UV radiation on cells, these processes can only be performed with extremely costly equipment. Thus, requirement (iii), low cost and high throughput, is advantageously fulfilled by our method, especially if compared to classical chip-based microfluidics, to three-dimensional bio-printing and to other additive manufacturing approaches [26,27].

To summarize, it appears that only our strategy can provide adequate encapsulation, sufficient manipulability and traceability of the encapsulated elements, and economically viable production—the conditions required to truly open up the path toward groundbreaking applications, such as the development of *ex-vivo* organ models or the establishment of efficient screening platforms. In this work, we apply our method with seven different liquid combinations and obtain seven differently prepared types of alginate fibers with average diameters ranging from 94 μm to 170 μm . To do so, we change not only the cross-linking agent (type of divalent cations), but also the relative amount of the various ingredients, including polyethylene glycol (PEG) and glycerol. By measuring the Young’s modulus and the elongation at break of these fibers, we demonstrate their good manipulability and identify the hydration level as the most critical parameter with respect to fiber elasticity. The paper is organized as follows. First we explain our strategy, briefly comparing it to existing alternatives. Then we specify the experimental setup and selected materials combinations. Before characterizing each fiber type, we discuss the equilibration conditions used to ensure the reproducibility of our measurements. Finally, we interpret our results and set out our conclusions.

II. PRODUCTION METHOD

A. General principle and comparison to existing approaches

To understand the specificity of our method, it is important to briefly review alternative approaches for fiber production. In so doing, one needs to keep in mind that none of them offers comparable geometry and dimension. The state of the art of fiber production relies on electrospinning, but only very few studies report sufficiently gentle process conditions for the cells to survive and sufficiently large electrospun fiber diameter for the cell to be encapsulated [28]. Coaxial electrospinning provides core-shell structures and emulsion electrospinning gives separated but irregular inclusions with variable and uncontrollable size, spacing, and shape [29–33]. To gain regularity, it has been proposed to first shape immiscible drops or plugs with classical microfluidic chips before injecting the compound jet in a vacuum [34,35]. This approach is, however, limited to micrometric liquid samples. Indeed, the solidification of the continuous jet, required to obtain a fiber, is a challenge as it requires its isolation from the micrometric channel walls. The strategy of choice is based on coaxial geometries where the outer fluid is immiscible with the core, which constitutes the fiber precursor. The sheath can be liquid [25] or gaseous [36] and can provide hydrodynamic focusing to reduce the fiber diameter or to increase the yield. Note that maximum flow rates are typically in the range from $O(1)$ to $O(10)$ ml h⁻¹ [25], thus significantly lower than with our method. Advanced coaxial configurations have led to more complex structures [37], however, the latter are always invariant along the fiber axis, excluding the possibility of forming physically separated cell clusters [15,38,39]. Furthermore, the narrow channels that are necessary to shape the coaxial flow are a source of viscous shear and can therefore only be used with low-viscosity fluids. This hinders the formulations of bioinks, especially when proteins of the extracellular matrix must be included. To overcome this challenge, which is often associated with undesired clogging, larger channels and nozzles have been employed, shifting the method from microfluidics toward extrusion [40,41] and further reducing the yields [27].

In contrast to these slow, complex and expensive processes, our method is based on IAMF. The idea is to replace the channels of a microfluidic device by a continuous liquid jet and to manipulate and combine the components (e.g., droplets from regular droplet streams) in air [23,42,43]. This does not require any carrying phase or channel and, consequently, clogging cannot occur. Moreover, thanks to the absence of viscous stresses at the channel walls, the throughput of IAMF can be orders of magnitude greater than that offered by classical microfluidic devices. This absence also implies that, for processing comparable volumes, IAMF requires much less energy

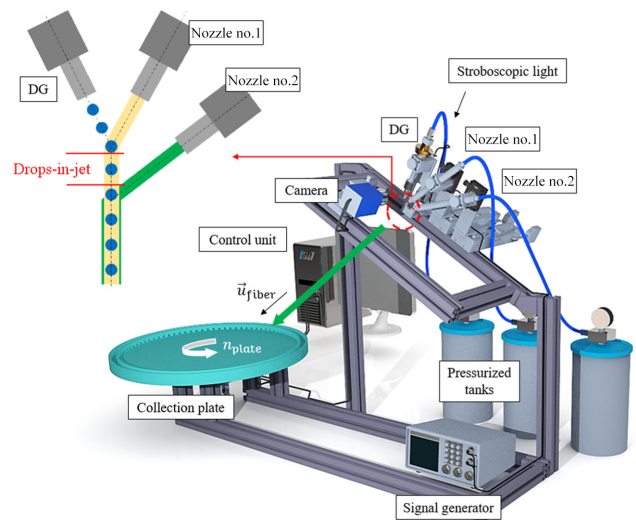


FIG. 1. Schematic illustration of the experimental setup (prototype) designed for the production of advanced fibers. (Left) Zoom into the two subsequent collisions respectively involving droplets (blue) and jet₁ (yellow), and the *drops-in-jet* structure with jet₂ (green). (Right) Overview of the various components enabling the controlled collisions and collection.

than standard chip-based technology. No expensive equipment is required, and the prototype (described in the following section) was built in house with a moderate budget [$O(10^4)$ euros]. More precisely, our production technique relies on two subsequent steps: the generation of a controlled liquid structure called *drops-in-jet* via IAMF, followed by its solidification via a sol-gel transition. The whole process takes place in air, where the resulting fibers are collected by a spinning disk. This principle and the associated prototype are depicted in Fig. 1; pictures taken during the process are shown later, in Fig. 2.

The geometry of the liquid structures produced by IAMF, their occurrence and stability have been studied in detail by our group [43,44]. The fragmentation of the drops within the continuous jet can be limited by reducing the drop inertia and by increasing the drop liquid viscosity and surface tension [45]. The fragmentation of the jet, which occurs if it is excessively deformed, can be prevented by increasing the jet liquid viscosity or by making it viscoelastic [46,47]. Thus, although we have chosen to fix here the drop and jet diameters to approximately 150 μm and 320 μm , respectively, other dimensions [typically ranging from $O(10)$ μm to $O(1)$ mm] could easily be reached. The engulfment of the droplets in the jet is favored by, but not strictly limited to, droplets whose diameter is equal to or smaller than that of the jet [43]. In our study, the drops are continuously produced by Plateau-Rayleigh instability, which offers typical drop spacing ranging from twice to four times the drop diameter. Using another drop formation technique, such as on-demand piezo-based inkjet, the

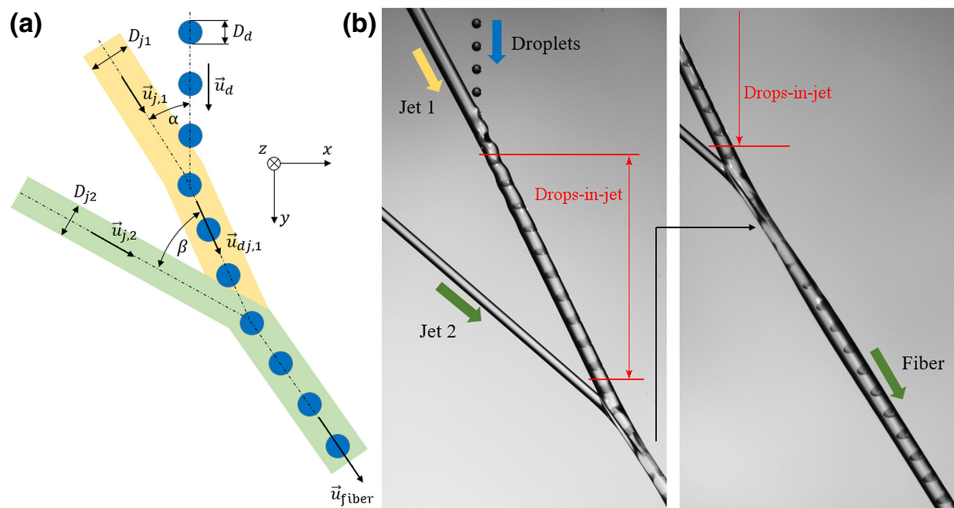


FIG. 2. (a) Kinetic and geometric parameters relevant for the production of fibers with regular inclusions. (b) Pictures of the collisions observed in the collision plane. The collisions between the droplets and jet₁ enable the formation of the liquid *drops-in-jet* structure, which subsequently solidifies thanks to the supply of cations ensured by the collision with jet₂.

spacing could be further varied, especially toward greater values.

Once the targeted *drops-in-jet* structure is produced, it is necessary to quickly and sufficiently solidify it to enable its damage free collection. “On the fly” ionic cross-linking had been successfully obtained with simple jets and complex drops obtained by IAMF to produce simple fibers, emulsions, suspensions, capsules, and Janus particles [36, 48,49]. Here, this strategy is adapted by introducing an additional jet, which supplies the required cations to the established *drops-in-jet* structure, allowing its geometrical specificity to be maintained based on the presence of regularly spaced monodisperse inclusions. In this way, fibers can be produced with a throughput in the range of approximately 1400 ml h^{-1} (i.e., $17\,000 \text{ m}$ of fiber per hour), and thus several order of magnitudes greater than those reported by previously mentioned “on the fly” approaches [48]. This very high production rate makes the damage-free collection of the fibers difficult. The entry of fragile fibers into liquid baths or their impact on static solid surfaces generates excessive stresses and irremediably leads to loss of their physical integrity. As detailed in the next section, this challenge has been successfully overcome by adding a specifically designed spinning disk.

B. Prototype and parameters

The prototype enabling the fiber production comprises three pressurized tanks for the separate supply of the drop and jet liquids (see Fig. 1). The air pressure inside each of the three tanks and, related thereto, the flow rates of the three liquids are independently adjusted using an OB1 MK3+ pressure controller from Elveflow (Paris, France).

The droplet stream is generated with a droplet generator (DG) following the well-known Plateau Rayleigh instability [50,51], while the two jets are created using simple nozzles (nozzle no. 1 and nozzle no. 2). The first jet (jet₁, yellow), made of an aqueous alginate solution, constitutes the basis of the fiber. The regularly impacting droplets (blue) are in turn building the regular inclusions of the future fiber. Thus, it is essential that the droplets are regularly embedded in the first jet, and that neither the droplets nor the jet fragment. The collision parameters are therefore adjusted to stably provide the desired *drops-in-jet* regime (see the red section in Figs. 1 and 2). In order to achieve an in-flight sol-gel transition of the *drops-in-jet* structure generated, a second jet (jet₂, green) is needed, which immediately covers the previously formed compound (droplets + jet₁) and supplies the divalent cations to initiate the cross-linking reaction. Details of the liquid compositions can be found in Sec. III. By temporarily stopping the drop stream, it is therefore possible to temporarily suppress the inclusions in the fiber. Similarly, different droplet streams can be used to produce inclusions of different sizes, with different spacings, or to encapsulate different actives or cells.

In the present setup, the DG is fixed, while the two nozzles are mounted on microtraverses for an accurate adjustment enabling, *inter alia*, the suppression of any off-plane eccentricity. A camera with a resolution close to $4 \mu\text{m}$ per pixel provides detailed collision pictures in the collision plane. The collisions are illuminated from the back using a stroboscopic light, which is connected to the same signal generator as the droplet generator in order to produce standing pictures. Here, the frequency is set to $f_d = 15\,500 \text{ Hz}$ for all tested liquid combinations. The DG has a fixed orifice diameter, $D_{\text{orifice}} = 100 \mu\text{m}$, and the two

jets are created using two nozzles from Vieweg GmbH (Germany) with inner diameters $D_{\text{nozzle},1} = 340 \mu\text{m}$ and $D_{\text{nozzle},2} = 230 \mu\text{m}$, respectively. The relevant kinetic and geometric parameters [shown in Fig. 2(a)] are extracted from the collision pictures [see Fig. 2(b)]. These parameters do not change much when testing the different liquid combinations. The diameters of the droplets and the jets are typically in the range of $D_d = 150 \pm 10 \mu\text{m}$, $D_{j,1} = 320 \pm 5 \mu\text{m}$, and $D_{j,2} = 213 \pm 5 \mu\text{m}$. Here, the subscripts $d, j, 1$ and $j, 2$ stand for the droplet, the first and the second jet, respectively. The two collision angles, α and β , are set to $25.5 \pm 1.5^\circ$ and $28 \pm 2^\circ$, respectively. The absolute value of the droplet velocity, given by $\vec{u}_d = \vec{L}_d f_d$, is $6.7 \pm 0.8 \text{ m s}^{-1}$, where \vec{L}_d is the distance between two consecutive droplets. The two flow-rate equivalent jet velocities $|\vec{u}_{j,1}|$ and $|\vec{u}_{j,2}|$ are measured and both are found to be $5.0 \pm 0.2 \text{ m s}^{-1}$. Further, the velocity of the generated structure \vec{u}_{fiber} , is estimated via a momentum balance and is found to remain in the range of $5.0 \pm 0.2 \text{ m s}^{-1}$. The relative impact velocities $\vec{U}_1 = \vec{u}_d - \vec{u}_{j,1}$, between droplets and jet₁, and $\vec{U}_2 = \vec{u}_{j,2} - \vec{u}_{d,j,1}$, between jet₂ and droplets + jet₁, are calculated providing values of $3.0 \pm 0.5 \text{ m s}^{-1}$ and $1.9 \pm 0.2 \text{ m s}^{-1}$, respectively. The impact Weber numbers of the subsequent collisions, that is, of the droplets with respect to jet₁, $We_d = \rho_d D_d U_1^2 / \sigma_d$, and of the *drops-in-jet* with respect to jet₂, $We_{j,2} = \rho_{j,2} D_{j,2} U_2^2 / \sigma_{j,2}$, remain below 35 for all tested liquid combinations. These small values of We_d , in combination with $L_{j,1}/D_{j,1} = u_{j,1}/(D_{j,1} f_d) \approx 1$ obtained for all sets of experiments, ensure that the *drops-in-jet* structure is stably established for all investigated collisions, despite the usage of low-viscosity liquids [45,46].

It is important to note that the continuous monitoring of the off-plane eccentricity and of the preset collision parameters during the production process is supported by a software application involving the control unit, the camera, and the automated (motorized) microtraverses. Finally, the fibers generated must be collected without inducing too much stress and strain. At this early production stage, the fibers are made of wet hydrogels, which are fragile and easily stretchable, requiring soft handling. The collection system therefore consists of a horizontal plate mounted on a brushless motor, which is connected to the control unit. The speed of the spinning plate, n_{plate} , is controlled to match that of the fiber at its impact point \vec{u}_{fiber} . After the fibers are collected, they are allowed to dry at room temperature before further process steps follow. Details can be found in Sec. IV B.

III. MATERIALS AND LIQUID PROPERTIES

A. Combinations investigated

Several studies on alginate-based fibers show that their mechanical properties are strongly affected by the manufacturing conditions, the molecular weight and the

structure of the sodium alginate, the type of cross-linking agent, possible additives and their concentrations in the solutions, as well as by the time of contact between the cross-linking agent and the alginate [52,53].

Thoroughly testing all these effects would go far beyond the scope of this work. Instead, we focus on the most relevant parameters, investigating seven different types of fibers, whose production conditions are listed in Table I. The precise composition of each solution and corresponding properties are given in the next section. Using preliminary results (not shown), we first define a reference fiber (fiber ref in Table I). This fiber contains inclusions formed by droplets and is produced with calcium ions as cross-linking agent, with PEG as plasticizer and without any subsequent post-treatment (i.e., relying only on the sol-gel transition happening in air).

To test the influence of the contact time between the cross-linking agent and sodium alginate, a fiber similar to the reference fiber is produced and placed, immediately after collection, in a liquid bath. The bath contains the same solution as jet₂. The residence time of the fibers in the bath is fixed to 5, 10, or 30 min. The resulting fibers are named fiber bath 5 min, fiber bath 10 min, and fiber bath 30 min, respectively (see Table I).

Next, a fiber without inclusions is produced (fiber w/o drops in Table I). Practically, the same conditions as for the reference fiber are used but the droplet stream is switched off, leaving only jet₁ and jet₂ interact.

In order to evaluate the influence of a plasticizer on the mechanical properties of the hydrogel, we prepare for jet₁, a sodium alginate solution without PEG. Different studies show that PEG blended with sodium alginate can modify the elasticity of the resulted fiber, which further affects its Young's modulus as well as its elongation at break [54,55]. The corresponding fiber is called fiber w/o PEG in Table I.

Finally, the influence of the cross-linking agent is investigated. Thus, we replace the widely used calcium chloride (CaCl_2), which provides calcium cations, by strontium chloride (SrCl_2), which supplies the strontium cations at similar concentration. Note that whatever the cross-linking agent, it is always present both in jet₂ and in the droplets. Thus, to obtain this last fiber, called fiber SrCl_2 in Table I, we change both the droplet liquid and that of jet₂.

B. Solution composition and properties

(a) Jet₁ or alginate solution

In this study, the molecular weight of the sodium alginate (low molecular weight, low viscosity) and its concentration are kept constant for all tested liquid combinations. Note that the exact molecular weight of the sodium alginate cannot be provided by the supplier. To avoid uncontrolled variations, the same batch is used throughout the study. The sodium alginate selected, purchased from Sigma Aldrich, USA, as low-viscosity alginic acid

TABLE I. Different fiber types tested in this study and the corresponding conditions used for their production. Liquid combination and composition for droplets, jet_1 , jet_2 , and liquid bath (if any).^a

	Liquids						
	Droplets		Alg	Jet ₁	Jet ₂		Bath
	G5 + CaCl ₂	G5 + SrCl ₂			Alg w/o PEG	EtOH + CaCl ₂	
1. Fiber ref	x	—	x	—	x	—	—
2. Fiber bath 5 min	x	—	x	—	x	—	x
3. Fiber bath 10 min	x	—	x	—	x	—	x
4. Fiber bath 30 min	x	—	x	—	x	—	x
5. Fiber w/o drops	—	—	x	—	x	—	—
6. Fiber w/o PEG	x	—	—	x	x	—	—
7. Fiber SrCl ₂	—	x	x	—	—	x	—

^ax = yes; — = no.

sodium salt from brown algae with 39% G-block and 61% M-block, allows us to use reasonably high concentrations while keeping the solution dynamic viscosity moderate (see Table II). The chosen concentration has been specified via extensive preliminary studies using different types of sodium alginates.

For the reference fiber, the alginate solution, Alg, further contains polyethylene glycol 20 000 ($M_w \approx 20\,000\text{ g mol}^{-1}$ from Carl Roth GmbH, Germany), both being dissolved in a mixture of distilled water and ethanol (from Carl Roth GmbH, Germany). The mass fractions of the four components (sodium alginate, PEG, water, and EtOH) are 3.5%, 1.5%, 85%, and 10%, respectively.

The second alginate solution used for jet_1 , Alg w/o PEG, is similar to Alg except that no PEG is added. Thus, the mass fractions of the three components (sodium alginate, water, and EtOH) are 3.5%, 86.5%, and 10%, respectively.

The addition of ethanol was motivated by its ability to promote, via surface tension reduction, the encapsulation of the droplets [48] and to improve the mechanical properties of the hydrogel network [56]. Yet, we observed (but do not show) that droplet encapsulation is preserved in the absence of surface tension difference and that the most

relevant parameter influencing the mechanical properties of the hydrogel is its hydration level (see Sec. V). Thus, we expect that the removal of ethanol from jet_1 would not modify the results presented.

(b) Droplets or G5 solution

It is important to mention that, the cross-linking agents are added not only to the liquid of the second jet but also to that of the droplets. The reasons for this are twofold. First, it supports the in-flight solidification of the alginate solution, making it sufficiently fast to collect the fibers. In practice, the distance between the collision point and the collection plate is approximately 1 m, which leads for typical fiber velocities $u_{\text{fiber}} \approx 5\text{ ms}^{-1}$ to an available solidification time of only 200 ms. Even though the gelation transition of sodium alginate is known to be fast compared to other gelation processes [57], it is preferable to initiate it from both the inside (via the droplets) and the outside (via jet_2) of the main jet (jet_1). Second, the divalent cations added to the droplets help to fix the shape and position of the droplets (inclusions) inside the jet made of alginate solution as regularly as possible. Indeed, the three liquids, which are brought into contact, are miscible. To limit the diffusion of the droplet liquid into the jet_1 liquid, and reciprocally, it is advantageous to trigger additional and quasi-instantaneous gelation upon the contact between them.

For the drop liquids (G5 + CaCl₂ and G5 + SrCl₂), we use an aqueous glycerol solution with a mass fraction of glycerol ($\geq 98\%$ purity, Carl Roth GmbH, Germany) in distilled water (Kerndl GmbH, Germany) of 50%. The addition of glycerol was used to economically increase the liquid viscosity toward the value expected for bioink and could be replaced in subsequent tests by PEG (not shown). In order to test the influence of the cross-linking agent, we add CaCl₂ (Carl Roth GmbH, Germany) and SrCl₂ (in the form of strontium chloride hexahydrate, SrCl₂ 6H₂O, $\geq 99\%$ purity p.a., Carl Roth GmbH, Germany) both with the same concentration of 1 mol l^{-1} to the droplet liquid

TABLE II. Properties of the liquids used in this study. All measurements were carried out at ambient conditions of $T = 23 \pm 1\text{ }^\circ\text{C}$ and $\text{RH} = 40 \pm 3\%$.

Liquid	Density ρ (g dm ⁻³)	Dynamic (mPa s) viscosity μ	Surface tension σ (mN m ⁻¹)
G5 + CaCl ₂	1187.5	7.9	65.2
G5 + SrCl ₂	1210.1	5.7	65.8
Alg	997.4	53.1	45.5
Alg w/o PEG	996.6	39.3	45.5
EtOH + CaCl ₂	981.6	3.3	26.6
EtOH + SrCl ₂	1035.1	3.2	27.3

G5. Keep in mind that 1 mole of strontium chloride hexahydrate contains the same number of strontium atoms as 1 mole of pure SrCl_2 , which, in turn, is equal to the number of calcium atoms in 1 mole of CaCl_2 . Thus, the concentrations are comparable. The droplet liquids are dyed with rhodamine B (C.I.45170, Merck, USA).

(c) Jet_2 or cross-linking solution

The two aqueous solutions of jet_2 ($\text{EtOH} + \text{CaCl}_2$ and $\text{EtOH} + \text{SrCl}_2$) are used to probe the influence of the different divalent cations as cross-linking agent. Calcium chloride and strontium chloride are added with the same concentration as for the droplet liquids (1 mol l^{-1}). The aqueous solution, which is used for both liquids, is a mixture of distilled water and ethanol with a mass ratio of 50% : 50%. This high concentration of ethanol is used to strongly increase the surface tension difference $\Delta\sigma$ between jet_1 and jet_2 , which leads to a quick coating of jet_1 by jet_2 and thus promotes a uniform solidification. As mentioned already, depending on the needs of the application, and especially if cells are used, other chemicals could be used to lower the surface tension.

(d) Bath

When a liquid bath is used, its composition is the same as that of jet_2 . Thus, in the presently tested configurations, it consists of a water and ethanol mixture at 50 : 50 (w : w), in which CaCl_2 is dissolved at a concentration of 1 mol l^{-1} . It is referred to as $\text{EtOH} + \text{CaCl}_2$.

For completeness, the values of the surface tension σ , the density ρ , and the dynamic viscosity μ of all previously listed liquids are shown in Table II. The density is measured by weighing an exact volume of 100 ml (graduated flask and analytical scale), the viscosity is determined with a glass capillary viscometer, and the surface tension is measured with the pendant drop method.

IV. FIBER CHARACTERIZATION

In this work, the regularity of the fibers is first optically assessed. Then the fibers are characterized by their mechanical properties and, more precisely, by their elongation at break, ϵ , and Young's modulus, E (see the Appendix for details of the methods). To guarantee reproducibility, all measurements are carried out after the fibers have been preconditioned. This step involves storing the fibers under controlled conditions (temperature and humidity) for a minimum period of time until they equilibrate with these conditions. This conditioning step is justified by the evolution of ϵ and E observed right after fiber collection.

A. Optical control of regularity

One of the key points of our method compared to classical electrospinning approaches is the regularity of the fibers produced. These have a cylindrical shape with a constant diameter. Further, when inclusions are present, they

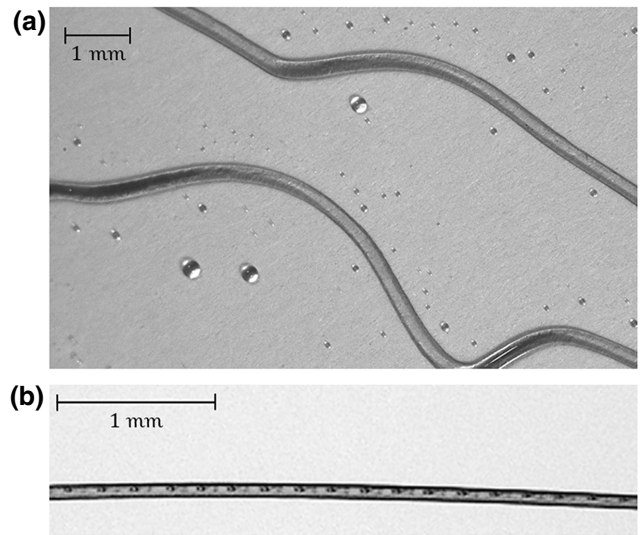


FIG. 3. Recorded picture of (a) samples of fiber w/o drops in wet state showing its uniformity immediately after collection and (b) a sample of the reference fiber with regular inclusions in dry state.

have a well-defined size and spacing period. To control the regularity of the fibers, we image them and measure their diameter. We thoroughly and consistently obtained variations of less than 5% per sample and therefore do not present or discuss the data further. Figure 3 illustrates this aspect with pictures of (a) fibers w/o drops showing the uniformity of the generated fibers immediately after the collection, and (b) the reference fiber with regular inclusions in equilibrated state.

B. Fiber preconditioning

After the different types of fibers are produced, similar temperature and humidity conditions are applied in order to obtain reliable and comparable measurements of their characteristics. Indeed, immediately after the fibers are collected, their hydration level is quite high and their wet state is a source of difficulties for reproducible characterization. This aspect is known and different studies show that the mechanical properties strongly deviate when measuring the same fiber or gel in dry and wet state [58–61].

To characterize this variability, we first follow the evolution of the reference fiber properties during the first instants after its collection (i.e., in its wet state). The information obtained in this way motivates the preconditioning of the fibers. The duration of preconditioning is determined in a second step, by measuring the fiber diameter, as explained at the end of this section. In all experiments, the conditions in which the fibers are left to equilibrate correspond to the ambient conditions of our laboratory, which are controlled. During the whole study, the temperature is found to be $T = 23 \pm 1 \text{ }^\circ\text{C}$ and the relative humidity $\text{RH} = 40 \pm 3\%$.

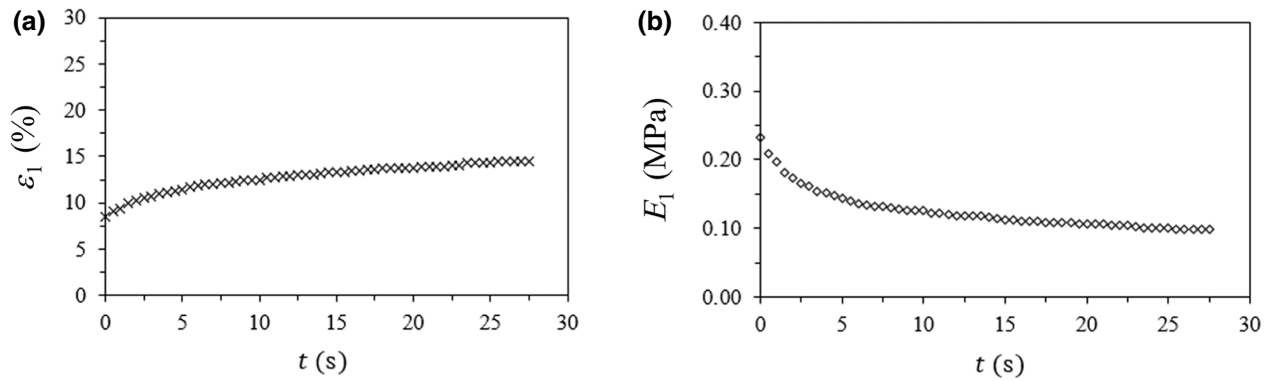


FIG. 4. (a) The elongation with a fixed weight (approximately constant stress) ϵ_1 and (b) the pseudo Young's modulus E_1 as a function of time of the fiber reference type in the wet state, that is, immediately after the production and collection.

To follow the evolution of the fiber properties during its first instants, the wet fiber is, immediately after collection, clamped horizontally in the measurement device described in the Appendix. To enable better control of the fiber “age,” the measurements are performed by a team of two operators. A single freshly produced sample is used in combination with a single weight, which, hung on the middle of the fiber, produces a fixed stress. The temporal evolution of the fiber elongation, $\epsilon_1(t)$, and its pseudo Young's modulus, $E_1(t)$, are followed, taking the instant when the weight has been added as time origin $t = 0$ s. Here, the pseudo Young's modulus designates the instantaneous strain-stress ratio but does not strictly correspond to the Young's modulus, the fiber being inelastic. The results are plotted in the form of $\epsilon_1(t)$ and $E_1(t)$ in Figs. 4(a) and 4(b), respectively. Shortly after the stress has been applied, the fiber continuously deforms and, as a result, ϵ_1 , and E_1 vary. This can be attributed to the fact that the fiber behaves like a wet viscoelastic hydrogel [62,63] and not like a solid network, and that the residual water, which is stored in the wet fiber, evaporates during the measurement procedure, leading to a change of the fiber hydration level. This continues until an equilibrium state between the fiber and the surrounding environment is reached. These observations make it almost impossible to meaningfully compare the different types of fibers in their wet state. Thus, we decide to let the fibers fully equilibrate with the controlled laboratory conditions, before further characterizations are done.

In order to define the minimum drying or preconditioning period at ambient conditions, we produce five samples of fiber w/o drops (see Table I). These samples are placed, directly after collection, on a water-repellent substrate (solid substrate covered with a polypropylene foil) and their diameters are measured at regular intervals with the help of a camera. Figure 5(a) shows an example of the fiber w/o drops (fiber 3, diamonds) in wet ($t = 0$ min) and dry state ($t_{\text{dry}} > 12$ min). The diameters of the five samples D , normalized by their diameters in dry state D_{dry} , are plotted

as a function of time in Fig. 5(b). The equilibration rate is similar for all five samples before reaching the steady-state plateau, which happens after $t_{\text{dry}} \approx 12$ min. From then on, the fiber diameter does not further change, which supports the assumption that the equilibrium state is reached. Note that the time period of $t_{\text{dry}} \approx 12$ min is defined as the minimum fiber equilibrating time after collection for all types of fibers produced within this study. In practice, we always characterize fibers after they equilibrate for more than 60 min.

V. RESULTS AND DISCUSSION

In this section we focus on the Young's modulus, E , and the elongation at break, ϵ , of the different fiber types listed in Sec. III. The characterization procedures are explained in the Appendix and all measurements are carried out at ambient conditions with fibers equilibrated for at least 12 min (after t_{dry}). The fibers are produced, collected, and hung to equilibrate in air (laboratory conditions), leading to a uniform sample dehydration.

A. Young's modulus

The Young's moduli of the seven differently prepared fibers and their diameters are shown in Fig. 6. Here, at least five samples of each type are characterized and the average (gray) as well as the maximum (dark blue) and minimum (light blue) values are plotted. The error bars represent the standard deviations obtained on the measurement ensemble of at least five points. This representation is motivated by the fact that the E -values of various samples of one fiber type are found to deviate. The reasons are probably diverse and cannot be definitively identified. For example, and despite images showing very regular structures, one cannot totally exclude microscopic imperfections in these structures. Other homogeneities (e.g. of the equilibrating or cross-linking processes) could also cause these deviations. Despite careful adjustment of the collecting plate velocity with that of the fibers, small differences cannot be

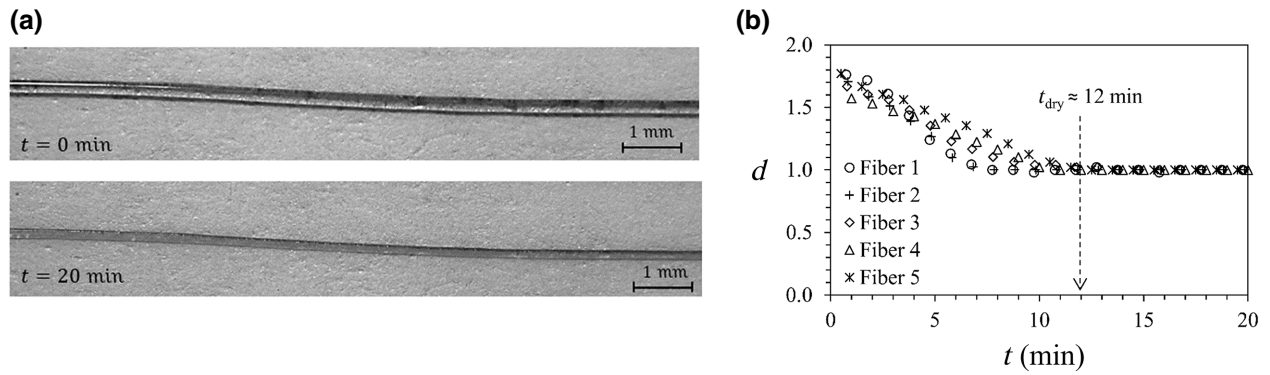


FIG. 5. (a) Recorded pictures of a fiber w/o drops in wet ($t = 0 \text{ min}$) and dry state (after $t_{\text{dry}} > 12 \text{ min}$, at $T = 23 \pm 1 \text{ }^\circ\text{C}$ and $\text{RH} = 40 \pm 3\%$). (b) The temporal evolution of the normalized fiber diameter $d = D/D_{\text{dry}}$ of five fiber samples after collection.

avoided, which may stretch the fibers and thus modify their mechanical properties. Similarly, damage produced while placing the fragile fiber in the measurement device, especially at the clamping sites, is expected to affect the results. Such damage is limited by gentle handling of the fibers and the smooth surface of the clamping parts but cannot be totally eliminated. Finally, we identify the hanging of the weights as another potential source of localized but critical damage. The latter is indeed not relevant to our study but could constitute a large source of noise. Note that the hypothesis of local damage (either from clamping or by hanging the weights) is supported by the comparable low data dispersion obtained for elongation at break. For measuring the elongation at break, no weight is used and only fibers which break away from the two clamping points are analyzed.

The maximum Young's modulus of the reference fiber (with regular inclusions and without CaCl_2 bath) $E_{\text{fiber ref}}$ is found to be about 45 MPa in this work. It is important to note that a cross-study comparison of E obtained for different alginate-based fibers is extremely difficult, due to the large amount of influencing factors. The fiber preparation, additives, molecular weights, cross-linking time, hydration level, etc. strongly affect the mechanical properties, as already demonstrated. The Young's modulus of alginate-based fibers can vary by several order of magnitudes, for example between 0.2 MPa [64] if produced with a classical microfluidic device and 6 GPa [65] if obtained by a wet spinning technique. Other factors, which may lead to large differences in values of the Young's modulus, may be the measurement device/technique itself, as well as the fact that the stress-strain relation of the fiber may not always be thoroughly linear. In the work by Cuadros *et al.* [64], who used a Universal Texture Analyser TA.XT2i (Godalming, Surrey, UK) in tension mode, the stress-strain relation of alginate fibers is clearly linear until the fiber fractures. Note that in our device, we obtain linear strain-stress curves. Small deviations are observed at origin, which are caused by a small prestrain of the fiber

when fixing it, and before loading it. Other studies, such as those of Zhang *et al.* [66] and McNamara *et al.* [59], who used a tensile tester XQ-1C (Shanghai, China) and an Instron Universal Testing machine model 5569 (Canton, MA, USA) respectively, show partly and even strongly nonlinear strain-stress curves. This, of course, questions the relevance of the deduced Young's modulus. Thus, quantitative comparison of the Young's modulus is only made for the results obtained within this study (i.e., for fibers produced with the same method and characterized with the same device and protocol). Discussion, including results from other groups, remains at a qualitative level.

Placing the reference fiber, just after collection from the spinning disk, in a liquid bath containing CaCl_2 for 5, 10, and 30 min, significantly decreases the Young's modulus, while increasing the fiber diameter. The Young's modulus is reduced by as much as a factor of 10 if the fiber is immersed 5 min in a CaCl_2 bath. This reduction continues if the fiber is left longer in the bath. Yet, the effects seem to saturate. After 30 min and more (data not shown), the Young's modulus remains close to 1 MPa. Thus, averaged over the first 5 min and over the last 20 min, the

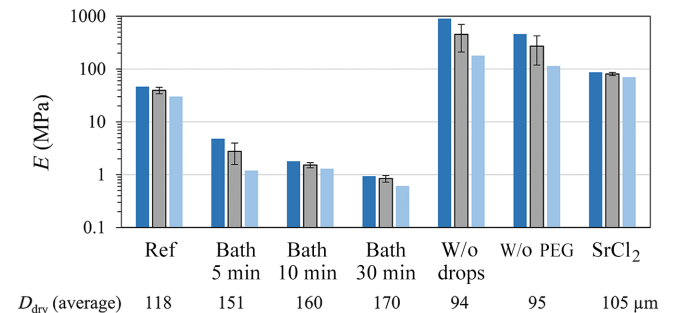


FIG. 6. The Young's modulus, E , and average dry diameter obtained on at least five samples for each of the seven fiber types studied. The average values with the standard deviation (error bar) are shown in gray, while the maximum (minimum) values are shown in dark (pale) blue.

decrease rate is found to be approximately 8 MPa min^{-1} and $0.04 \text{ MPa min}^{-1}$, respectively. Similarly, the effects on the diameter are more important during the first 5 min. During this period, D_{dry} increases by 28%, thus with an average rate of more than 5% per minute while during the last 20 min, the diameter changes only by less than 6%, which corresponds to an average rate of less than 0.3% per minute. Note that the strain obtained with the highest stress (approximately 0.10 N mm^{-2}) starts to deviate from the linear curve, probably indicating the transition from the elastic toward the plastic domain. These evolutions can be attributed to the hygroscopic behavior of CaCl_2 [67] in combination with the different retention times in the liquid bath. The longer the retention time, the more divalent calcium cations diffuse into the alginate network. Thanks to the higher calcium content and its hygroscopic behavior, more water is present and the hydration level of the fiber remains high, even if the fiber is left to equilibrate with room conditions for several hours, a phenomenon referred to as water retention rate of sodium alginate fibers [68]. The large diameters simply correspond to higher content of residual water in the fibers. This is confirmed by the comparison of the lineic weight of the fibers. After drying, the reference fiber has a lineic weight of approximately $10 \mu\text{g m}^{-1}$, while that of the fibers, first placed in a liquid bath for 30 min, increases to about $27 \mu\text{g m}^{-1}$. Yet, after some time in the bath, the adsorption of calcium cations reaches its maximum and saturates, explaining why the magnitude of these effects is stabilizing after 30 min. To understand the evolution of the Young's modulus, it is important to note that the "hydrated" fibers behave rather like hydrogels and not like solidlike networks. Consequently, the increase in the fiber diameter is concurrent with the strong decrease in the Young's modulus down to less than 1 MPa and the earlier mentioned transition toward a plastic response. McNamara *et al.* [59] also found that wet alginate fibers have a much weaker Young's modulus than their dry counterparts, an effect attributed to the plasticizer role of water in biopolymer fibers [69]. In general, different studies also observed that wet fibers are more fragile and plastic than the same fibers characterized in the dry state [60,61]. This point is further discussed at the end of this section, where Fig. 7 shows the variations in the averaged values of E with the averaged equilibrated diameters, D_{dry} , that is, at first order, with the gel hydration level.

Fibers w/o drops (meaning without inclusions) show smaller diameters than those with inclusions. This is expected since the materials carried by the droplets are now missing. This effect is already visible while looking at the corresponding liquid structures, namely *drops-in-jet* and *jet₁*, (see for example, the central pictures of Fig. 2 or those by Planchette *et al.* [43]). Yet, the effect is much more pronounced once the fibers are left to equilibrate. Indeed, looking at Fig. 2 or considering continuity, the

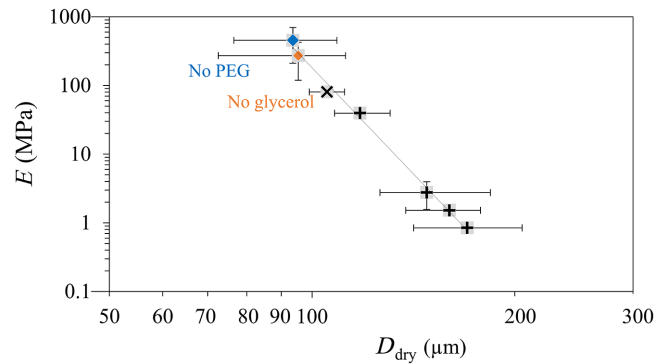


FIG. 7. Average Young's modulus, E , as a function of the average diameter of the equilibrated fiber, D_{dry} . Same data as in Fig. 6; the fibers without drop/PEG are marked with blue/orange diamonds; black +/× indicates the presence of $\text{Ca}^{2+}/\text{Sr}^{2+}$. The continuous line shows the correlation given by $E = 6 \times 10^{22} D_{\text{dry}}^{-11}$, the error bars represent the standard deviations.

liquid section (or liquid diameter) ratio without and with droplets is found to be around 0.94 (or 0.97), much closer to 1 than the same ratio obtained comparing the section (or diameter) of the equilibrated fibers, namely 0.51 (or 0.71). This is probably caused by the composition of the droplet liquid, which contains, beside calcium cations, an important amount of glycerol (50% by weight). Indeed, glycerol is known to be hygroscopic and its presence in the gel leads to an increased retention of water, similarly to what happens when more Ca^{2+} is adsorbed. Consequently, and as expected, the value of E is increased in the absence of droplets. With a maximum of about 900 MPa, it corresponds to the stiffest tested fiber.

Fibers w/o PEG (i.e., fibers without PEG but with regular inclusions) show a significantly smaller diameter than the reference type with PEG. As already observed for the fibers left in a Ca^{2+} bath and for those made without droplets, this decrease in diameter is accompanied by an increase in the Young's modulus. This might be attributed to the hygroscopic properties of PEG, which is at the origin of greater hydration level in equilibrated fibers [70]. Thus, in the absence of PEG, the water retention decreases and, consequently, the Young's modulus increases. These results are also in agreement with several studies showing that using polyethylene glycol (or any hygroscopic plasticizer) leads to a reduction in the Young's modulus [71–74].

Finally, by replacing Ca^{2+} with Sr^{2+} , we observe a smaller but comparable diameter of $105 \mu\text{m}$ instead of $118 \mu\text{m}$ for the reference fiber. The variation in the Young's modulus is significant, with a maximum increasing from 45 MPa to 80 MPa (more than 70%) but remains of the same order of magnitude. Using fracture curves, Zhang *et al.* report more robust mechanical performance of strontium-alginate fibers compared to calcium-alginate

ones [66,75]. However, the published stress-strain curves being nonlinear, no Young's modulus value is given, preventing any direct comparison. In our case, we cannot exclude that the increase in E obtained by using Sr^{2+} is caused by the decrease in the fiber hydration, indirectly measured by D_{dry} .

To clarify this point, the previous data are plotted in Fig. 7 in the form of E versus D_{dry} . The error bars represent the standard deviations obtained on the measurements of at least five different samples for each fiber type. Interestingly, for all studied fibers, a strong correlation between E and D_{dry} can be found, which is well represented by the function $E = 6 \times 10^{22} D_{\text{dry}}^{-11}$ (continuous gray line). Thus, it seems that the variations in the Young's modulus are primarily caused by the changes in D_{dry} , and therefore, at first order, by the variations in the hydration level. This interpretation is in agreement with the results of Olivas *et al.* [73] who showed that whatever the gel composition, their hydration level, tuned by conditioning under variable relative humidity, is the parameter most influencing their mechanical properties. More particularly, the authors reported that the higher the hydration, the lower the Young's modulus. Replacing Ca^{2+} with Sr^{2+} may lead to further variation in E but this seems negligible compared to the effects of D_{dry} .

The results obtained without PEG also indicate a decrease in the water retention correlated with an increase in the Young's modulus, in qualitative agreements with other studies [71–73].

When glycerol is missing (i.e., in the absence of droplets), a similar trend is observed: the average dry diameter is reduced and the measured value of E increased, following the previously mentioned correlation given by $E = 6 \times 10^{22} D_{\text{dry}}^{-11}$. Glycerol being known to increase the water retention of alginate gel [72,74], our interpretation is similar to that for PEG. Like Gao *et al.* [74], we observe greater effects for PEG than for glycerol. Yet, when present in our experiments, glycerol has a weight percentage 2.3 times larger than PEG, making this comparison irrelevant. Interestingly and more importantly, while the structure of the fiber with and without droplets is different, no significant deviations from the previously mentioned correlation are found. This may indicate that the presence of inclusions, probably associated with local composition gradients, do not have strong effects on the fiber elasticity. Further, it is important to keep in mind that our data have some uncertainty, which calls for careful interpretation rather than definitive conclusions.

B. Elongation at break

Let us now take a closer look at the elongation at break, ϵ , of the fibers. Here again we test at least five samples of each type and keep the average value, which is plotted in gray with the minimum and maximum values in dark and

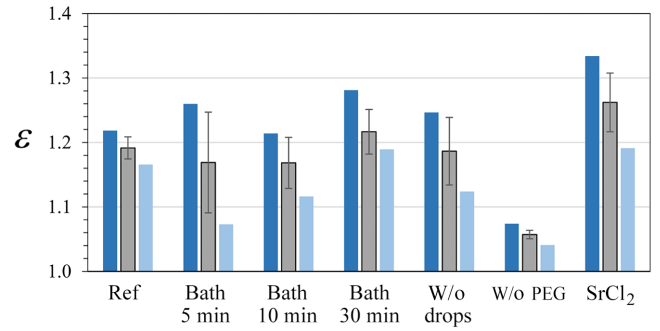


FIG. 8. The elongation at break, ϵ , of the seven different types of fibers. For each type, the average value (gray) with standard deviation, as well as the maximum and minimum values (dark and pale blue) obtained for at least five samples are given.

pale blue, respectively (see Fig. 8). The error bars indicate the standard deviations for all measured samples on each fiber type. As already mentioned, for these measurements, we only evaluate fibers which break in between the two clamping points, which automatically eliminates the possible errors mentioned for the Young's modulus and partly attributed to undetected damage at the clamping positions. Avoiding strong clamping, however, also induces the possibility that the fibers are held too weakly and thus slide a little, producing another type of measurement error.

The breaking elongation of the reference fiber remains in the range of $18 \pm 5\%$, which is comparable to the breaking elongation of alginate-based fibers including PEG found in the literature. Wang *et al.* [54] obtained a breaking elongation between 19% and 24% for sodium alginate fibers ($M_v = 120\,000 \text{ g mol}^{-1}$) containing PEG6000 with mass fractions between 2% and 10%. Keeping the fiber in a liquid bath containing CaCl_2 does not significantly increase this value. In contrast, replacing Ca^{2+} by Sr^{2+} increases the elongation at break up to $26 \pm 6\%$. The observed average breaking elongation therefore increases by a factor of 1.4 compared to the reference case. Similar results were obtained by Zhang *et al.* [66] who reported an increase in the breaking elongation of pure sodium alginate fibers cross-linked with strontium ions by the factor of about 1.6 compared to fibers cross-linked with calcium ions. The effect is attributed to the stronger ionic bonding of the strontium cations with the carboxylic group of the alginate molecules. It is therefore expected that not exactly the same factor is found with a different type of alginate [66,75].

The most dramatic effect on the breaking elongation is caused by the removal of PEG (see fibers w/o PEG). The elongation at break decreases to values of about $5\% \pm 2\%$. The absence of the plasticizer leads to more rigid fibers, which consequently break at smaller deformations. For comparable composition, similar values are reported in the literature, where ϵ ranges between 4% and 9% [54,66,68].

Finally, it seems that inclusions do not have any notable effect on the elongation at break, as suggested by the values obtained for fibers w/o drops. This observation may result from two contrary effects that roughly cancel each other out. As seen in Fig. 6 and reported in the literature [73,74], glycerol has a plasticizing effect and is therefore expected to increase the elongation at break. Thus, its removal, which stems from the absence of droplets, should significantly reduce ϵ . Simultaneously, this absence also leads to a more regular fiber, in which no inclusions are present. The latter can be seen as localized defects and thus as sources of local stress inhomogeneities, which can trigger the rupture. To put it another way, the absence of inclusions is expected to increase the elongation at break, which is in practise not observed. We thus make the hypothesis that the two previously mentioned effects (absence of plasticizer and absence of local inhomogeneities)- more or less cancel each other out. To go further, additional experiments are needed, which could for example use droplets but without any glycerol and would include the localization of the rupture point relative to the inclusion positions. This goes beyond the purpose of our work.

VI. CONCLUSIONS

We have experimentally investigated how fibers with and without regular inclusions can be produced via the in-flight collision of a regular droplet stream and two liquid jets. The throughput could be increased by an order of magnitude (approximately 1500 ml h^{-1}) compared to the highest value reported by other research groups working on fiber production via IAMF. We designed an experimental setup or prototype which allows an online feedback loop on the droplets and jet alignment, and enables us to smoothly collect the generated fibers at velocities of about 5 ms^{-1} . The available time span between the collision point of the three liquids and the collection plate is of the order of 200 ms, fairly short compared to the solidification time offered by other fiber production technologies, but sufficient to produce uniform fibers with comparable mechanical properties. In this study we tested seven different liquid combinations, whereby the average diameters of the fibers, allowed to equilibrate under controlled laboratory conditions, were found to be between $94 \text{ }\mu\text{m}$ and $170 \text{ }\mu\text{m}$. To manufacture these fibers with regular inclusions, we used droplets with $D_d \approx 150 \text{ }\mu\text{m}$ consisting of aqueous glycerol solutions containing SrCl_2 or CaCl_2 , which collided with the first liquid jet. The jet was based on aqueous sodium alginate solutions, with and without polyethylene glycol, with a diameter of about $320 \text{ }\mu\text{m}$. The second jet, with a diameter of about $210 \text{ }\mu\text{m}$, consisted of aqueous solutions also containing SrCl_2 or CaCl_2 . To generate the fibers, the sol-gel transition of the sodium alginate jet was initiated from the inside, via the droplets, and from the outside, via the second jet, by means of ionic

cross-linking triggered by divalent cations, here Sr^{2+} and Ca^{2+} . After the collected fibers were left to equilibrate, their mechanical properties, namely Young's modulus and elongation at break, were determined with the help of a measurement device manufactured in-house.

The maximum Young's modulus and the elongation at break of the reference fiber were found to be 45 MPa and $18 \pm 5\%$, respectively. This fiber was obtained using sodium alginate and PEG in combination with CaCl_2 as cross-linking agent in the droplets and the second jet. Placing similar fibers in a liquid bath containing the liquid of the second jet (aqueous solution of CaCl_2), however, drastically reduced the Young's modulus, by about an order of magnitude, while the elongation at break did not seem to be significantly affected. This effect was attributed to the hygroscopic behavior of CaCl_2 , which led to highly hydrated fibers even after equilibration with the room conditions. Wet fibers generally show weaker mechanical properties than their dry counterparts. Sodium alginate fibers with PEG and without inclusions, as well as pure sodium alginate fibers without PEG but with inclusions, had the two greatest elasticity moduli obtained in this study, respectively close to 900 MPa and 460 MPa. As expected, the absence of either glycerol or PEG, well-known hydrophilic plasticizers, increased the Young's modulus values. As in other studies, the concurrent decrease in the water retention seems to indicate that this effect is directly correlated to the hydration level of the hydrogel. The absence of either PEG or glycerol, however, did not have the same effects on the elongation at break. Without PEG but with inclusions, the elongation at break was found to be very small, around $5 \pm 2\%$, which can be explained by the absence of PEG's plasticizing effect. When droplets were removed, no significant variation in the elongation at break was measured. This may simply result from stronger plasticizing effects of the PEG in comparison to the glycerol. This could also be caused by two contrary effects, namely the lack of glycerol's plasticizing action and the suppression of stress inhomogeneities probably developing around the inclusions. Further experiments should help clarifying this point. Finally, SrCl_2 was used for cross-linking the reference alginate solution containing PEG. In this case, the breaking elongation could be increased by a factor 1.40, while the increase in the Young's modulus by a factor 1.77 rather seemed to be caused by the reduced hydration level.

ACKNOWLEDGMENTS

We would like to thank the Austrian Science Fund (FWF; Grant No. P31064-N36) and the Austria Wirtschaftsservice Gesellschaft mbH (AWS; Patent No. EP 3412801 B1) for their financial support.

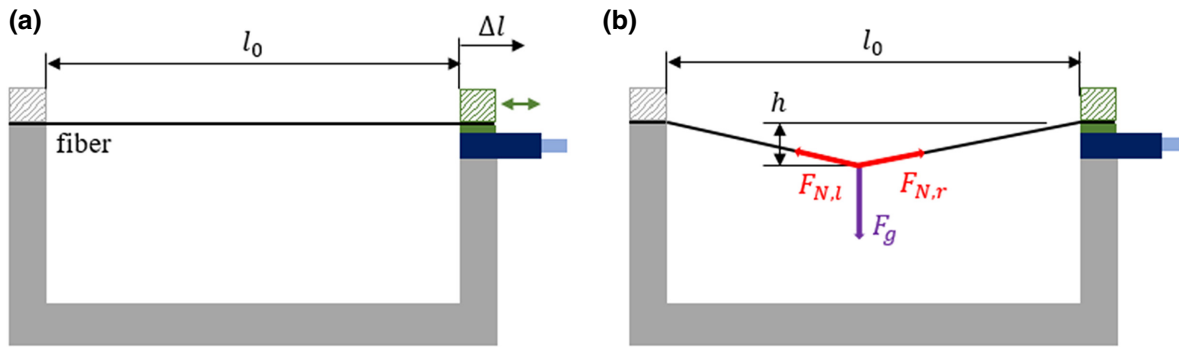


FIG. 9. Measurement principle and sketch of the device used for the determination of the elongation at break ϵ (a), and Young's modulus E (b).

APPENDIX: FIBER CHARACTERIZATION METHODS

To obtain the elongation at break, ϵ , and the Young's modulus, E , we use the same measurement device, which was designed and built in-house. Schematic illustrations are shown in Fig. 9. The device consists of a base (gray, fully colored), which is fixed, and a one-axis microtraverse (blue, fully colored) mounted on the base. The cross-hatched areas indicate the two parts, which are used to clamp the fibers. Further, the green-colored elements, attached to the microtraverse, can be moved by operating it. It is important to note that all edges with which the fibers may come into contact are rounded off to eliminate irregularities, which could damage the fibers. For the same reason, surfaces clamping the fibers are well polished.

For the measurement of the elongation at break $\epsilon = l_b/l_0$, the fiber is carefully clamped in the measurement device, whereby slacking must be avoided [see Fig. 9(a)]. At this point, a camera is used to measure the initial length of the fiber l_0 . After that, the samples are quasistatically elongated with the help of the microtraverse until the fiber breaks. The whole elongation process is videorecorded for an accurate determination of the breaking point. The breaking length of the fiber $l_b = l_0 + \Delta l$ is measured with the help of the last recorded frame showing an intact fiber.

The determination of the Young's modulus $E = \Delta\sigma/\Delta\epsilon$ is performed with the same device [see Fig. 9(b)]. This parameter quantifies the slope of the stress-strain diagram of a certain elastic material. Here, σ stands for the normal stress in the fiber. At the beginning, the fiber is again carefully clamped in the measurement device, whereby slacking must be avoided, and a picture is taken to estimate l_0 . In the next step, the first weight m_1 is placed in the middle of the fiber (at about $l_0/2$) and another picture is recorded. The added weight leads to an elongation of the fiber ϵ_1 , while the fiber is subjected to a force $F_{g,1} = m_1g$. The elongation corresponding to m_1 can be calculated as $\epsilon_1 = (1 + 4h_1^2/l_0^2)^{1/2} - 1$. The weight force $F_{g,1}$ is balanced by tensions $F_{N,l}$ and $F_{N,r}$ on each side of

the fiber. In the case of symmetry, $F_{N,l} = F_{N,r} = F_1$ and the induced stress can be calculated as $\sigma_1 = F_1/A$, where $A = D^2\pi/4$ defines the cross section of the fiber and D is the fiber diameter. This procedure is carried out by using five weights in total with an increasing mass from m_1 to m_5 , varying between 0.0312 g and 0.5017 g. This leads to a stress-strain diagram including five data points for each fiber. By fitting these points with a linear function, the Young's modulus E can be estimated. To ensure that the stretching of the fiber is in the range of an elastic deformation, pictures are taken after each weight is removed from the fiber. These pictures are used to control the fully elastic relaxation of the fiber to its initial stage. Note that the linear fitting function of the stress-strain relation usually shows a small positive intercept (i.e., a nonzero stress at l_0). This can be attributed to some prestrain of the fiber. In order to compensate this slight offset, l_0 is corrected and, consequently, the respective measured strain values are slightly modified. The resulting Young's modulus values, however, do not change significantly when implementing this correction since it represents a variation of less than 0.5%.

- [1] F. Berthiaume, T. J. Maguire, and M. L. Yarmush, Tissue engineering and regenerative medicine: history, progress, and challenges, *Annu. Rev. Chem. Biomol. Eng.* **2**, 403 (2011).
- [2] A. R. Herman, The history of skin grafts, *J. Drugs Dermatology* : JDD **1**, 298 (2002).
- [3] K. Dzobo, N. E. Thomford, D. A. Senthebane, H. Shipanga, A. Rowe, C. Dandara, M. Pillay, and K. S. C. M. Motaung, Advances in regenerative medicine and tissue engineering: Innovation and transformation of medicine, *Stem Cells Int.* **2018**, 2495848 (2018).
- [4] S. K. Doke and S. C. Dhawale, Alternatives to animal testing: A review, *Saudi Pharm. J.* **23**, 223 (2015).
- [5] M.-H. Wu, S.-B. Huang, and G.-B. Lee, Microfluidic cell culture systems for drug research, *Lab Chip* **10**, 939 (2010).

- [6] M. W. Laschke and M. D. Menger, Life is 3D: Boosting spheroid function for tissue engineering, *Trends Biotechnol.* **35**, 133 (2017).
- [7] O. Frey, P. M. Misun, D. A. Fluri, J. G. Hengstler, and A. Hierlemann, Reconfigurable microfluidic hanging drop network for multi-tissue interaction and analysis, *Nat. Commun.* **5**, 1 (2014).
- [8] E. Brouzes, M. Medkova, N. Savenelli, D. Marran, M. Twardowski, J. B. Hutchison, J. M. Rothberg, D. R. Link, N. Perrimon, and M. L. Samuels, Droplet microfluidic technology for single-cell high-throughput screening, *Proc. Natl. Acad. Sci.* **106**, 14195 (2009).
- [9] A. Kang, J. Park, J. Ju, G. S. Jeong, and S.-H. Lee, Cell encapsulation via microtechnologies, *Biomaterials* **35**, 2651 (2014).
- [10] G. Orive *et al.*, Cell encapsulation: Promise and progress, *Nat. Med.* **9**, 104 (2003).
- [11] R. Langer and D. A. Tirrell, Designing materials for biology and medicine, *Nature* **428**, 487 (2004).
- [12] T. Andersen, P. Auk-Emblem, and M. Dornish, 3D cell culture in alginate hydrogels, *Microarrays* **4**, 133 (2015).
- [13] G. H. Lee, J. S. Lee, X. Wang, and S. Hoon Lee, Bottom-up engineering of well-defined 3D microtissues using microplatforms and biomedical applications, *Adv. Healthc. Mater.* **5**, 56 (2016).
- [14] J. W. Nichol and A. Khademhosseini, Modular tissue engineering: Engineering biological tissues from the bottom up, *Soft Matter* **5**, 1312 (2009).
- [15] H. Onoe *et al.*, Metre-long cell-laden microfibres exhibit tissue morphologies and functions, *Nat. Mater.* **12**, 584 (2013).
- [16] V. Trivedi, A. Doshi, G. Kurup, E. Ereifej, P. Vandevord, and A. S. Basu, A modular approach for the generation, storage, mixing, and detection of droplet libraries for high throughput screening, *Lab Chip* **10**, 2433 (2010).
- [17] T. S. Kaminski, O. Scheler, and P. Garstecki, Droplet microfluidics for microbiology: Techniques, applications and challenges, *Lab Chip* **16**, 2168 (2016).
- [18] N. Hao, Y. Nie, and J. X. Zhang, Microfluidics for silica biomaterials synthesis: Opportunities and challenges, *Biomater. Sci.* **7**, 2218 (2019).
- [19] E. Dressaire and A. Sauret, Clogging of microfluidic systems, *Soft Matter* **13**, 37 (2017).
- [20] M. Hassanpourfard, R. Ghosh, T. Thundat, and A. Kumar, Dynamics of bacterial streamers induced clogging in microfluidic devices, *Lab. Chip.* **16**, 4091 (2016).
- [21] A. Dewan, J. Kim, R. H. McLean, S. A. Vanapalli, and M. N. Karim, Growth kinetics of microalgae in microfluidic static droplet arrays, *Biotechnol. Bioeng.* **109**, 2987 (2012).
- [22] M. Kato-Negishi, J. Sawayama, M. Kawahara, and S. Takeuchi, Cell fiber-based 3D tissue array for drug response assay, *Sci. Rep.* **12**, 1 (2022).
- [23] C. Planchette, G. Brenn, and H. Hinterbichler, Method for producing a regular arrangement of droplets of a first liquid in a continuous jet of a second liquid, European Patent **EP 3412801 B1** (2020).
- [24] Y. Song, D. Cheng, L. Zhao, and K. F. Lei, in *Introduction: The Origin, Current Status, and Future of Microfluidics*, edited by Y. Song, D. Cheng and L. Zhao (2018), Online ISBN: 9783527800643.
- [25] S.-J. Shin, J.-Y. Park, J.-Y. Lee, H. Park, Y.-D. Park, K.-B. Lee, C.-M. Whang, and S.-H. Lee, “on the fly” continuous generation of alginate fibers using a microfluidic device, *Langmuir* **23**, 9104 (2007).
- [26] M. Rothbauer, C. Eilenberger, S. Spitz, B. E. Bachmann, S. R. Kratz, E. I. Reihs, R. Windhager, S. Toegel, and P. Ertl, Recent advances in additive manufacturing and 3D bioprinting for organs-on-a-chip and microphysiological systems, *Front. Bioeng. Biotechnol.* **10**, 837087 (2022).
- [27] J. Ma, Y. Wang, and J. Liu, Bioprinting of 3D tissues/organs combined with microfluidics, *RSC. Adv.* **8**, 21712 (2018).
- [28] S. N. Jayasinghe, Unspooling the history of cell electrospinning, *Matter* **5**, 4 (2022).
- [29] H. Qi, P. Hu, J. Xu, and A. Wang, Encapsulation of drug reservoirs in fibers by emulsion electrospinning: Morphology characterization and preliminary release assessment, *Biomacromolecules* **7**, 2327 (2006).
- [30] A. Moghe and B. Gupta, Co-axial electrospinning for nanofiber structures: Preparation and applications, *Polym. Rev.* **48**, 353 (2008).
- [31] A. Yarin, Coaxial electrospinning and emulsion electrospinning of core-shell fibers, *Polym. Adv. Technol.* **22**, 310 (2011).
- [32] X. Hu, S. Liu, G. Zhou, Y. Huang, Z. Xie, and X. Jing, Electrospinning of polymeric nanofibers for drug delivery applications, *J. Control. Release* **185**, 12 (2014).
- [33] A. M. Al-Enizi, M. M. Zagho, and A. A. Elzatahry, Polymer-based electrospun nanofibers for biomedical applications, *Nanomaterials* **8**, 259 (2018).
- [34] M. L. Grünbein and G. Nass Kovacs, Sample delivery for serial crystallography at free-electron lasers and synchrotrons, *Acta Crystallogr. Sect. D: Struct. Biol.* **75**, 178 (2019).
- [35] A. Echelmeier *et al.*, Segmented flow generator for serial crystallography at the European x-ray free electron laser, *Nat. Commun.* **11**, 4511 (2020).
- [36] R. Vasireddi, J. Kruse, M. Vakili, S. Kulkarni, T. F. Keller, D. C. Monteiro, and M. Trebbin, Solution blow spinning of polymer/nanocomposite micro-/nanofibers with tunable diameters and morphologies using a gas dynamic virtual nozzle, *Sci. Rep.* **9**, 14297 (2019).
- [37] Y. Cheng, F. Zheng, J. Lu, L. Shang, Z. Xie, Y. Zhao, Y. Chen, and Z. Gu, Bioinspired multicompartamental microfibers from microfluidics, *Adv. Mater.* **26**, 5184 (2014).
- [38] C. Colosi, S. R. Shin, V. Manoharan, S. Massa, M. Costantini, A. Barbetta, M. R. Dokmeci, M. Dentini, and A. Khademhosseini, Microfluidic bioprinting of heterogeneous 3D tissue constructs using low-viscosity bioink, *Adv. Mater.* **28**, 677 (2016).
- [39] K. Ikeda, S. Nagata, T. Okitsu, and S. Takeuchi, Cell fiber-based three-dimensional culture system for highly efficient expansion of human induced pluripotent stem cells, *Sci. Rep.* **7**, 2850 (2017).
- [40] W. Jia *et al.*, Direct 3D bioprinting of perfusable vascular constructs using a blend bioink, *Biomaterials* **106**, 58 (2016).
- [41] D. N. du Chatinier, K. P. Figler, P. Agrawal, W. Liu, and Y. S. Zhang, The potential of microfluidics-enhanced extrusion bioprinting, *Biomicrofluidics* **15**, 041304 (2021).
- [42] c. Planchette, H. Hinterbichler, and G. Brenn, Drop stream - immiscible jet collisions: Regimes and fragmentation

- mechanisms, Proceedings of the 28th Conference on Liquid Atomization and Spray Systems (2017).
- [43] C. Planchette, S. Petit, H. Hinterbichler, and G. Brenn, Collisions of drops with an immiscible liquid jet, *Phys. Rev. Fluids* **3**, 093603 (2018).
- [44] D. Baumgartner, R. Bernard, B. Weigand, G. Lamanna, G. Brenn, and C. Planchette, Influence of liquid miscibility and wettability on the structures produced by drop-jet collisions, *J. Fluid. Mech.* **885**, A23 (2020).
- [45] D. Baumgartner, G. Brenn, and C. Planchette, Effects of viscosity on liquid structures produced by in-air microfluidics, *Phys. Rev. Fluids* **5**, 103602 (2020).
- [46] D. Baumgartner, G. Brenn, and C. Planchette, Universality of stretching separation, *J. Fluid. Mech.* **937**, R1 (2022).
- [47] D. Baumgartner, G. Brenn, and C. Planchette, Viscoelastic effects probed by drop-jet collisions, *Int. J. Multiphase Flow* **150**, 104012 (2022).
- [48] C. W. Visser, T. Kamperman, L. P. Karbaat, D. Lohse, and M. Karperien, In-air microfluidics enables rapid fabrication of emulsions, suspensions, and 3D modular (bio) materials, *Sci. Adv.* **4**, eaao1175 (2018).
- [49] T. Kamperman, V. D. Trikalitis, M. Karperien, C. W. Visser, and J. Leijten, Ultrahigh-throughput production of monodisperse and multifunctional Janus microparticles using in-air microfluidics, *ACS Appl. Mater. Interfaces* **10**, 23433 (2018).
- [50] G. Brenn, F. Durst, and C. Tropea, Monodisperse sprays for various purposes—their production and characteristics, *Part. Part. Syst. Charact.* **13**, 179 (1996).
- [51] U. Weierstall, Liquid sample delivery techniques for serial femtosecond crystallography, *Philos. Trans. R. Soc. B: Biol. Sci.* **369**, 20130337 (2014).
- [52] B. Niekraszewicz and A. Niekraszewicz, in *Handbook of textile fibre structure* (Woodhead Publishing, Cambridge, UK, 2009), p. 266.
- [53] K. Y. Lee and D. J. Mooney, Alginate: properties and biomedical applications, *Prog. Polym. Sci.* **37**, 106 (2012).
- [54] Q. Wang, N. Zhang, X. Hu, J. Yang, and Y. Du, Alginate/polyethylene glycol blend fibers and their properties for drug controlled release, *J. Biomed. Mater. Res. Part A* **82**, 122 (2007).
- [55] K. Dey, R. A. Khan, and A. S. Chowdhury, Study on the mechanical, degradation, and interfacial properties of calcium alginate fiber-reinforced polyethylene oxide composites, *J. Thermoplast. Compos. Mater.* **25**, 807 (2012).
- [56] E. Hermansson, E. Schuster, L. Lindgren, A. Altskär, and A. Ström, Impact of solvent quality on the network strength and structure of alginate gels, *Carbohydr. Polym.* **144**, 289 (2016).
- [57] J. Sun and H. Tan, Alginate-based biomaterials for regenerative medicine applications, *Materials* **6**, 1285 (2013).
- [58] D. I. Zeugolis, G. R. Paul, and G. Attenburrow, Cross-linking of extruded collagen fibers—a biomimetic three-dimensional scaffold for tissue engineering applications, *J. Biomed. Mater. Res. Part A: Off. J. Soc. Biomater., Jpn. Soc. Biomater., Aust. Soc. Biomater. Korean Soc. Biomater.* **89**, 895 (2009).
- [59] M. C. McNamara, F. Sharifi, J. Okuzono, R. Montazami, and N. N. Hashemi, Microfluidic manufacturing of alginate fibers with encapsulated astrocyte cells, *ACS Appl. Bio Mater.* **2**, 1603 (2019).
- [60] Y. Wei, S. Hudson, J. Mayer, and D. Kaplan, The crosslinking of chitosan fibers, *J. Polym. Sci. Part A: Polym. Chem.* **30**, 2187 (1992).
- [61] J. Li, Y. Wu, J. He, and Y. Huang, A new insight to the effect of calcium concentration on gelation process and physical properties of alginate films, *J. Mater. Sci.* **51**, 5791 (2016).
- [62] M. Mancini, M. Moresi, and R. Rancini, Mechanical properties of alginate gels: Empirical characterisation, *J. Food. Eng.* **39**, 369 (1999).
- [63] O. Chaudhuri, Viscoelastic hydrogels for 3D cell culture, *Biomater. Sci.* **5**, 1480 (2017).
- [64] T. R. Cuadros, O. Skurtys, and J. M. Aguilera, Mechanical properties of calcium alginate fibers produced with a microfluidic device, *Carbohydr. Polym.* **89**, 1198 (2012).
- [65] B. Sibaja, E. Culbertson, P. Marshall, R. Boy, R. M. Broughton, A. A. Solano, M. Esquivel, J. Parker, L. De La Fuente, and M. L. Auad, Preparation of alginate–chitosan fibers with potential biomedical applications, *Carbohydr. Polym.* **134**, 598 (2015).
- [66] X. Zhang, L. Wang, L. Weng, and B. Deng, Strontium ion substituted alginate-based hydrogel fibers and its coordination binding model, *J. Appl. Polym. Sci.* **137**, 48571 (2020).
- [67] E. Vainio, N. DeMartini, L. Hupa, L.-E. Åmand, T. Richards, and M. Hupa, Hygroscopic properties of calcium chloride and its role on cold-end corrosion in biomass combustion, *Energy Fuels* **33**, 11913 (2019).
- [68] Q.-Q. Wang, Y. Liu, C.-J. Zhang, C. Zhang, and P. Zhu, Alginate/gelatin blended hydrogel fibers cross-linked by Ca^{2+} and oxidized starch: Preparation and properties, *Mater. Sci. Eng.: C* **99**, 1469 (2019).
- [69] B. A. Harper, Ph.D. thesis, University of Guelph, 2013.
- [70] J. A. Baird, R. Olayo-Valles, C. Rinaldi, and L. S. Taylor, Effect of molecular weight, temperature, and additives on the moisture sorption properties of polyethylene glycol, *J. Pharm. Sci.* **99**, 154 (2010).
- [71] L.-Y. Wang, W. F. Yong, E. Y. Liya, and T.-S. Chung, Design of high efficiency PVDF-PEG hollow fibers for air filtration of ultrafine particles, *J. Memb. Sci.* **535**, 342 (2017).
- [72] S. Wongchitphimon, R. Wang, R. Jiratananon, L. Shi, and C. H. Loh, Effect of polyethylene glycol (PEG) as an additive on the fabrication of polyvinylidene fluoride-co-hexafluoropropylene (PVDF-HFP) asymmetric microporous hollow fiber membranes, *J. Memb. Sci.* **369**, 329 (2011).
- [73] G. I. Olivas and G. V. Barbosa-Cánovas, Alginate–calcium films: Water vapor permeability and mechanical properties as affected by plasticizer and relative humidity, *LWT-Food Sci. Technol.* **41**, 359 (2008).
- [74] C. Gao, E. Pollet, and L. Avérous, Properties of glycerol-plasticized alginate films obtained by thermo-mechanical mixing, *Food Hydrocoll.* **63**, 414 (2017).
- [75] Ý. A. Mørch, I. Donati, B. L. Strand, and G. Skjak-Braek, Effect of Ca^{2+} , Ba^{2+} , and Sr^{2+} on alginate microbeads, *Biomacromolecules* **7**, 1471 (2006).